Energy & Environmental Science

ROYAL SOCIETY OF CHEMISTRY

PAPER

View Article Online
View Journal | View Issue

Cite this: *Energy Environ. Sci.*, 2024, **17**, 7932

Lithio-amphiphilic nanobilayer for high energy density anode-less all-solid-state batteries operating under low stack pressure†

Jihoon Oh, [ab] Seung Ho Choi, [c] Heejin Kim, [d] Ji Young Kim, [e] Geung-Jong Lee, [c] Ki Yoon Bae, [e] Taegeun Lee, [ab] Nohjoon Lee, [ab] Yeeun Sohn, [ab] Woo Jun Chung [ab] and Jang Wook Choi *[ab]

Received 16th July 2024,
Accepted 12th September 2024

DOI: 10.1039/d4ee03130j

rsc.li/ees

Anode-less all-solid-state batteries (ALASSBs) offer unparalleled energy density and enhanced safety. ALASSB cells usually incorporate a protective layer on the anode current collector to stabilize lithium (Li) deposition, yet are liable to short-circuiting even at low current densities. Here we report a nanobilayer comprising tungsten (W) and magnesium (Mg) with a total thickness of 230 nm for anode protection. The upper lithiophobic (Li-insoluble) W layer induces highly dense Li deposits underneath through its high interfacial energy, whereas the lower lithiophilic Mg layer nucleates Li for uniform Li deposition. Even at room temperature and low stack pressure (2 MPa), an energy density of 1100 W h L^{-1} and 71.9% retention after 300 cycles are demonstrated in a pouch-type full-cell. Furthermore, the effect of lithio-amphiphilicity is validated for other Li-insoluble metals, proving the versatility of the concept. This study unveils a simple yet effective approach for short-circuit-free cycling at high current densities, a challenging achievement for ALASSBs.

Broader context

Anode-less all-solid-state batteries (ALASSBs) eliminate the need for a specific host for lithium (Li) storage on the anode, enhancing volumetric energy density and substantially reducing cost. However, their progress is largely plagued by vulnerability to lithium (Li) dendrite growth, especially during fast charging. Micrometer-scale protective layers are usually employed to address this drawback but have proven effective only under high temperature and pressure conditions. This study introduces a bilayer approach in which a lithiophobic tungsten (W) layer is deposited on a lithiophilic (Mg) layer. Whereas the bottom Mg layer facilitates Li-ion migration downward for uniform deposition of Li, the top W layer induces dense cohesion of Li deposits without dendrite growth *via* its exceptionally high interfacial energy with Li. This lithio-amphiphilic bilayer enhances the practicality of ALASSBs by enabling fast charging, room-temperature, and low-pressure operation, alongside a high volumetric energy density of 1100 W h L^{-1}. This study exemplifies the concept of lithio-amphiphilicity for the first time for high-energy-density and practically viable ALASSBs.

Introduction

In the emerging era of electric mobility, the development of advanced secondary batteries with high energy density and superior resistance to ignition hazards is of paramount importance.[1,2] Along this direction, all-solid-state batteries (ASSBs) have emerged as a promising alternative to current commercial lithium-ion batteries (LIBs).[3,4] ASSBs not only provide enhanced safety against ignition by adopting non-flammable solid electrolytes (SEs) but also offer opportunities for using high-capacity anode materials such as metallic lithium (Li) to boost the energy density.[5,6] Among various classes of materials, sulfides are being intensively explored for SEs owing to their high ionic conductivity, which rivals that of their liquid electrolyte counterparts.[7–9] Additionally, the high

[a] *School of Chemical and Biological Engineering and Institute of Chemical Process, Seoul National University, 1 Gwanak-ro, Gwanak-gu, Seoul 08826, Republic of Korea. E-mail: jangwookchoi@snu.ac.kr*
[b] *Hyundai Motor Group-Seoul National University (HMG-SNU) Joint Battery Research Center (JBRC), Seoul National University, Seoul, Republic of Korea*
[c] *Advanced Batteries Research Center, Korea Electronics Technology Institute, Seongnam, Republic of Korea*
[d] *Division of Analytical Science, Korea Basic Science Institute, Daejeon, Republic of Korea*
[e] *Advanced Battery Development Team, Hyundai Motor Company, Hwaseong, Republic of Korea*

† Electronic supplementary information (ESI) available. See DOI: https://doi.org/10.1039/d4ee03130j

ductility of these sulfide materials facilitates continuous and sustained interparticle contact, even upon sintering at room temperature.[10–12]

In the pursuit of elevated energy density, extensive research focusing on the choice of anode materials and their electrode structures is currently underway.[13–16] Among the various approaches aiming to increase the energy density to its theoretical limits, anode-less ASSBs (ALASSBs) have stood out markedly.[17–19] However, the absence of an anode active material renders ASSB cells vulnerable to the growth of Li dendrites, which accelerate the performance degradation with cycling and restrict the operating conditions.[20,21] Researchers endeavoring to overcome this problem have explored covering the anode current collector with different types[22–25] of protective layers, with those comprising silver nanoparticles and carbon powder being the most representative.[26] In this protective layer, the silver nanoparticles serve as nucleation seeds for promoting uniform Li plating during charging, whereas carbon prevents direct contact between the SE and deposited Li to mitigate Li dendritic growth. Nonetheless, the majority of ALASSB cells either relies on relatively thick protective layers or requires operating conditions beyond those that are practically feasible in terms of temperature and pressure.[27] In a similar context, warranting short-circuit-free cycling at elevated current densities remains a challenge, and limits the rate capability. Moreover, the associated challenges related to uneven Li (de)plating over cycling compromise the volumetric energy density, the main motivation of the anode-less concept.

To address these chronic issues associated with ALASSBs, we propose a simple yet effective approach that involves the introduction of a thin bilayer consisting of magnesium (Mg) and tungsten (W) with a thickness of merely 230 nm. By employing an argyrodite-type sulfide SE, Li_6PS_5Cl (LPSCl), this nanobilayer accommodates remarkably high current densities of up to 5.0 mA cm^{-2} without short-circuiting. Furthermore, W/Mg-based pouch full-cells retain 71.9% of their original capacity after 300 cycles at room temperature and a low stack pressure of 2 MPa. The synergistic roles of the Mg and W layers unlock a useful design principle for developing high-performance ALASSBs, namely, the implementation of a lithio-amphiphilic protective layer.

Results and discussion

Plating-stripping behavior of the lithio-amphiphilic thin-film electrode

Although anode-less systems truly offer superior energy density compared to conventional cell configurations with active materials in the anodes (Fig. S1, ESI†), they often employ a protective layer with micrometer-scale thickness for sustainable cycling. In this regard, our electrode scheme, which entails wrapping the current collector with a metal layer that is several hundred nanometers thick, maximizes the benefits of the anode-less concept in terms of the energy density. In detail, we deposited a 30 nm-thick W layer on top of a 200 nm-thick Mg layer (Fig. 1(a)). Utilizing its lithiophilicity, the lower Mg layer induces uniform Li plating in the charging process by facilitating Li nucleation.[28,29] In contrast, the negligible solubility of Li in the upper W layer,[30] the origin of the mismatch in the surface energy between the two metals, prevents the indiscriminate penetration of the W layer by the deposited Li metal. Nevertheless, this W layer is sufficiently thin to allow the diffusion of Li ions without offering excessive resistance. Whereas the lithiophilicity of the Mg layer beneath provides a driving force for Li ion diffusion through the W layer, the presence of the W layer effectively prevents direct physical contact between the deposited Li during charge and the SE, thereby restricting the unwanted growth of the solid–electrolyte interphase (SEI). Important to note is that unstable SEI formation in ALASSB cells can severely accelerate capacity degradation because the entire supply of Li originates solely from the cathode material, unlike the use of Li metal foil, which supplies an excess amount of Li. The increased interfacial resistance resulting from unstable SEI formation also hinders fast charging and high power capabilities.[31] Consequently, the thin W layer stabilizes the anode–SE interface in multiple ways, particularly in operating scenarios involving high current densities.

The electrodes were fabricated by depositing a 200 nm-thick layer of elemental Mg onto a stainless steel (SUS) anode current collector using sputtering, followed by the additional sputtering of a 30 nm-thick layer of W. X-ray diffraction (XRD) analysis (Fig. S2, ESI†) revealed the (002) and (112) orientations to confirm the crystallinity of the Mg film. In the case of the bilayer, the (110) and (220) crystalline planes of W were additionally detected. Scanning electron microscopy with energy dispersive spectroscopy (SEM-EDS) images of the prepared Mg and W/Mg thin-film electrodes demonstrated that these elements were uniformly and evenly deposited (Fig. S3, ESI†). Time-of-flight secondary ion mass spectrometry (ToF-SIMS) depth profiling was utilized to precisely determine the thickness of the W/Mg bilayer structure (Fig. S4, ESI†).

Cross-sectional SEM-EDS images of the W/Mg thin-film electrode, acquired after Li plating, are presented in Fig. 1(b). This analysis revealed that Li was predominantly deposited beneath the W layer, and the overlapped Mg and Li distributions indicate that Li seamlessly amalgamated with the Mg therein. This supports that Li ions are able to diffuse through the W layer despite the inertness of W towards Li. Closer examination of the interface between the Li deposit and W layer divulged that, rather than wetting the underside of the lithiophobic W layer, the Li was deposited underneath this layer, where it densified (Fig. 1(b), magnified image). Cross-sectional SEM-EDS images captured after the Li was stripped revealed the repositioning of the dealloyed Mg beneath the W layer with detachment from neither the SE layer nor the current collector (Fig. S5, ESI†). This pointed to the structural stability of the W/Mg bilayer, a crucial requirement for long-term cycling. Additionally, XRD analysis of the W/Mg electrode after one cycle of Li plating and stripping (Fig. S6, ESI†) revealed the reaction behaviors of the Mg and W layers during Li (de)plating. Notably, the persistence of the W peak near 40° throughout

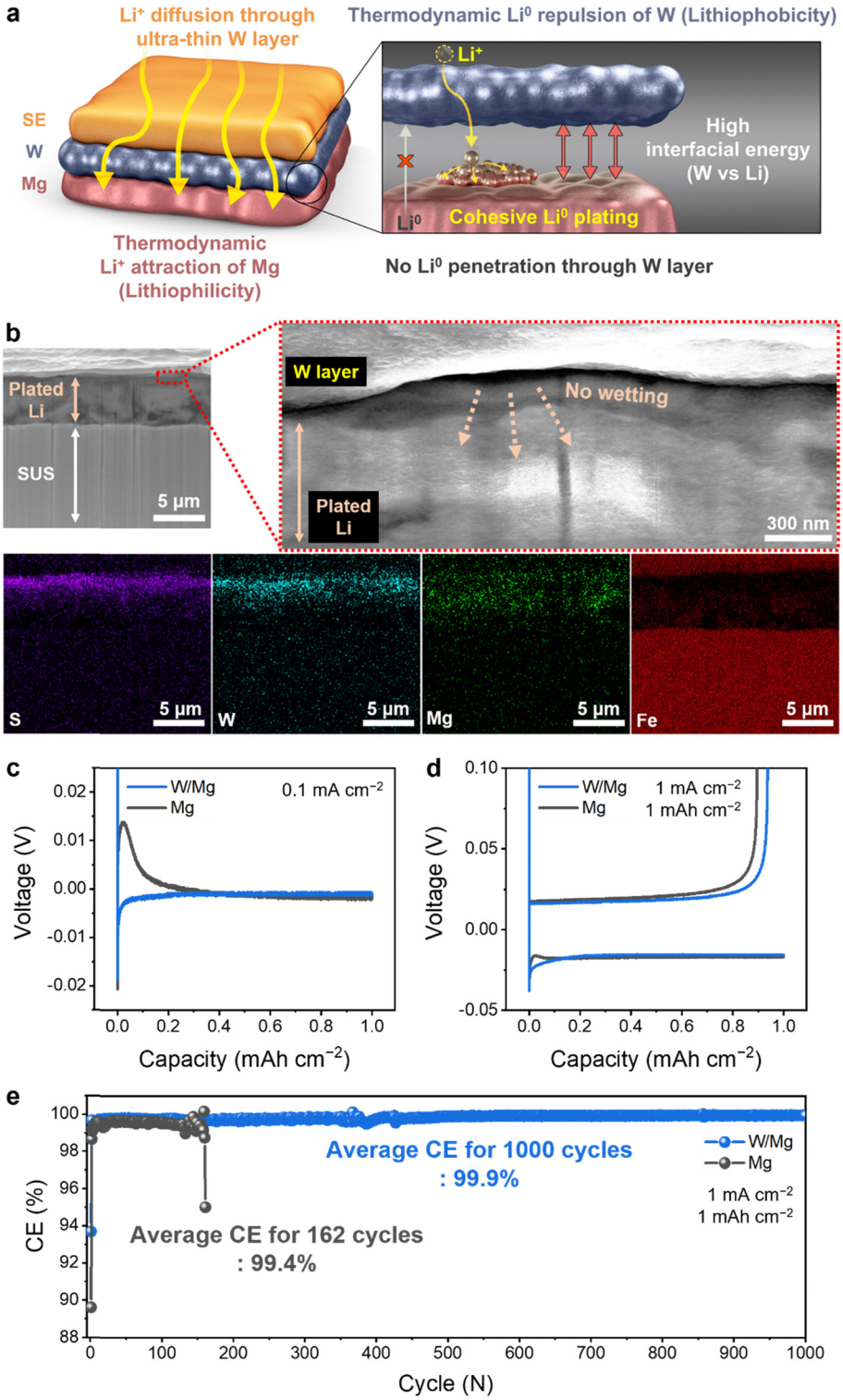

Fig. 1 Li plating-stripping behavior of the thin-film electrodes. (a) Schematic illustration of the charging process employing the W/Mg thin-film electrode. The Mg layer beneath the W layer promotes spatially uniform nucleation and Li deposition, whereas the W layer effectively suppresses dendritic growth. (b) Cross-sectional SEM-EDS images of the W/Mg thin-film electrode after Li plating at a current density of 1 mA cm^{-2} and a capacity of 1 mA h cm^{-2}, including (top right) a magnified SEM image to visualize the interface more vividly. The deposited Li is visible beneath the W layer and was fully amalgamated with Mg. (c) and (d) Half-cell plating-stripping tests of thin-film electrodes. Voltage profiles of the (c) plating processes with a current density of 0.1 mA cm^{-2} and (d) plating-stripping processes with a current density of 1 mA cm^{-2} and capacity of 1 mA h cm^{-2}. (e) CEs during half-cell evaluation with a current density of 1 mA cm^{-2} and a capacity of 1 mA h cm^{-2}. Preventing physical contact between the SE and the deposited Li not only limits SEI formation but also inhibits the dendritic growth of Li to improve the reversibility and cycle life.

Li plating and stripping provided direct evidence that W remains unreactive with Li by serving solely as an interfacial protective layer.

The lithiophilicity and lithiophobicity of Mg and W, respectively, were confirmed by examining the Li wettability using molten Li (Fig. S7, ESI†). By comparing two thin-film electrodes—one coated with only a 200 nm layer of Mg and the other with an additional 30 nm-thick layer of W on top (W(30 nm)/Mg(200 nm))—we observed that the molten Li completely wetted the Mg electrode (contact angle = 0°) to demonstrate its superior lithiophilicity. This uniform wetting facilitates stable Li plating during charging and is the thermodynamic driving force for Li ion diffusion through the W layer to the underlying Mg. In contrast, the molten Li placed on the W/Mg electrode did not wet the electrode at all, as was evident from the large contact angle (125°) (Fig. S8, ESI†). These observations are aligned with our electrode design scheme, which exploits the strong lithiophobicity of W to greatly prevent Li dendritic growth by inducing cohesive Li deposition underneath.

The electrochemical performance of the W/Mg bilayer thin-film was compared with its bare Mg counterpart by conducting all-solid-state half-cell plating-stripping tests using LPSCl as the SE. Initially, we monitored the voltage profiles of Li deposition at a current density of 0.1 mA cm^{-2} (Fig. 1(c)). The observed voltage dips at the initiation of Li deposition for both electrodes are reflective of Li nucleation. The lithiophilicity of the Mg thin-film was obvious from its voltage profile, which recovered to above 0 V immediately after the initial Li nucleation overpotential to indicate facile Li deposition (enlargements appear in Fig. S9, ESI†). In contrast, the overpotential of the W/Mg thin-film remained below 0 V following the initial voltage dip, attributed to the inertness of W towards Li, which hinders the diffusion of Li ions. However, it must be emphasized that this effect on the deposition was unsubstantial due to the limited thickness of the W layer of only 30 nm. This is evident from the even lower overpotential of W/Mg than that of bare Mg as the cumulative capacity exceeded 0.5 mA h cm^{-2}. This finding is in line with the role of W, namely to inhibit side reactions between the deposited Li and SE. This result persisted as the current density increased to 1 mA cm^{-2} (Fig. 1(d)). In the first cycle, the coulombic efficiencies (CEs) of W/Mg and Mg were conspicuously distinct at 93.7% and 89.6%, respectively. Subsequent plating-stripping cycles at 1 mA cm^{-2} and 1 mA h cm^{-2} resulted in higher CEs and a longer cycle life for W/Mg (Fig. 1(e)). This outcome highlights the role of the thin W layer in stabilizing the interface between the SE and the anode, thereby mitigating the loss of Li that would be otherwise utilized for significant side reactions with the SE.

Further evidence of the slight wetting of the interface of the W/Mg bilayer was gathered by subjecting thin-film electrodes with both the Mg and W/Mg layers and deposited Li to X-ray microscopy (XRM) imaging with micro-computed tomography (μ-CT) for two- and three-dimensional (2D and 3D) visualization (Fig. 2 and Fig. S10, ESI†). These visualizations revealed that, in the case of the bare Mg, the top surface of the Li deposition was mixed with the SE, indicating that Li had permeated through the SE layer as a result of Li dendritic growth (Fig. 2(a) and (c)). By contrast, the W/Mg bilayer prevented penetration of the SE layer to enforce compact, monotonic Li deposition

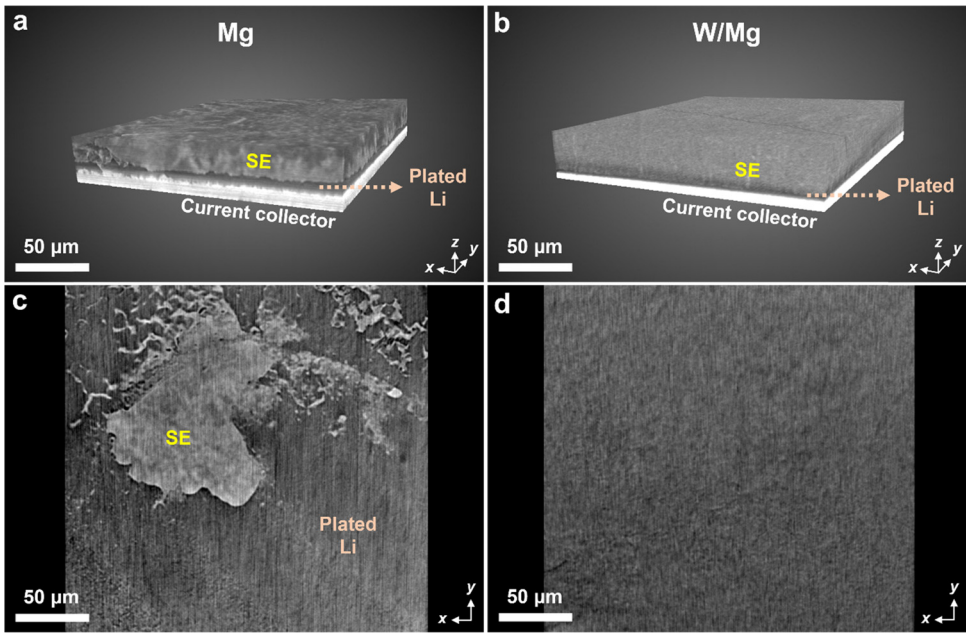

Fig. 2 3D and 2D XRM images of the thin-film electrodes with the Li depositions. (a) and (b) 3D images of anode-SE layers after Li plating on (a) Mg and (b) W/Mg thin-film electrodes. The black and brindled contrast in the SE layer in (a) reflects Li permeation therein and is attributed to dendritic growth. Conversely, in the case of W/Mg, the contrast in the SE layer was much weaker and more homogenous. (c) and (d) 2D images of the *x*–*y* plane across the topmost region of the Li deposits on the (c) Mg and (d) W/Mg thin-film electrodes. In the case of the Mg sample, the top of the deposited Li was mixed with the SE, indicative of its position within the SE layer.

(Fig. 2(b) and (d)). This result became more pronounced when the interfaces were magnified, and only the contrast corresponding to the SE was mapped (Fig. S11, ESI†).

Examining the voltage-*versus*-time curves from the corresponding half-cell assessments, by the second cycle, the voltage dip disappeared for both the Mg and W/Mg thin-film electrodes (Fig. S12, ESI†). This behavior is consistent with the typical pattern associated with Li nucleation in a lithiophilic layer.[32] In scenarios where nucleation occurs on a lithiophobic substrate, such as on the bare SUS current collector, the voltage dip persists beyond the second cycle (Fig. S13, ESI†). Therefore, the absence of the voltage dip serves as direct evidence that Li ions have effectively undergone nucleation within the underlying Mg layer after permeating through the W layer, a fact corroborated by the cross-sectional SEM and XRM images captured after Li deposition.

Assessment of anode–SE interfacial stability

The impact of the inhibitory effect of W on the anode–SE redox reaction was ascertained using X-ray photoelectron spectroscopy (XPS) and electrochemical impedance spectroscopy (EIS) analyses, both before and after 100 half-cell cycles. For Mg, the S 2p branch of XPS analysis exhibited a distinctive peak at around 160.8 eV, a higher binding energy than that of the P–S bond in the PS_4^{3-} of argyrodite sulfide SEs, indicating the reduction of sulfur to Li_2S—a well-known SEI component[33] (Fig. 3(a)). The presence of substantial Li_2S in Mg, contrary to the limited amount thereof in W/Mg, affirms the restricted

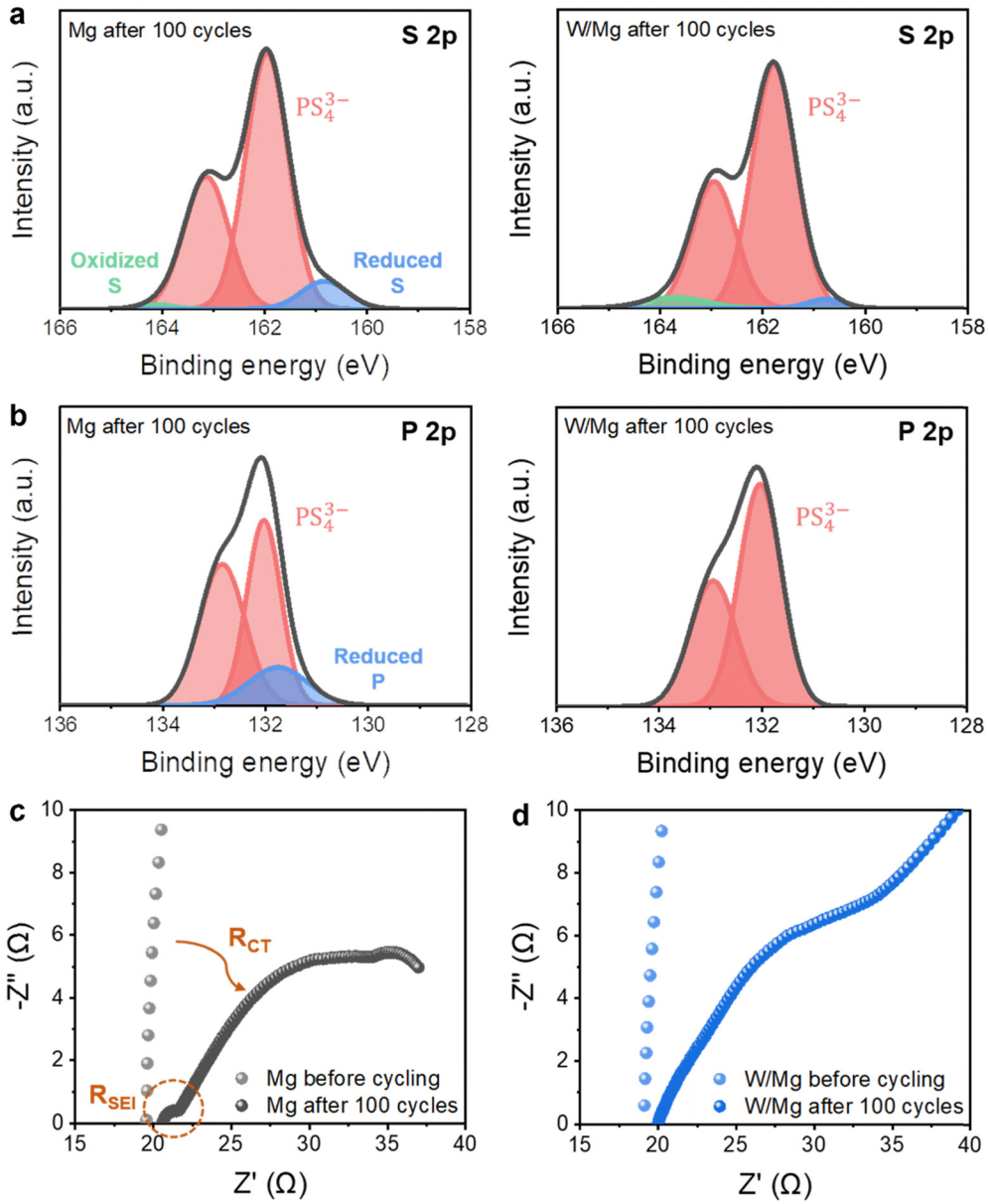

Fig. 3 Stability assessments of the anode–SE interface during half-cell operation. (a) and (b) XPS results of anode–SE interfaces after 100 cycles of half-cell evaluation, (a) S 2p and (b) P 2p spectra. (c) and (d) EIS Nyquist plots of the half-cells after 100 cycles with (c) Mg and (d) W/Mg thin-film electrodes.

direct contact between Li and the SE due to the presence of W at the interface. The P 2p branch displayed a similar trend, where, for Mg, the peak near 131.9 eV corresponds to the peak for Li_3P (Fig. 3(b)).[34] Li_3P is considered one of the less favorable SEI components, even more problematic than Li_2S, owing to its substantial electrical conductivity.[35] Enhanced electrical conductivity can trigger additional side reactions, which contribute to thickening the SEI.

Additionally, before cycling, the EIS Nyquist plots of both samples were approximately vertical, with only the bulk resistance (R_{bulk}) captured at the x-intercept (Fig. 3(c) and (d)). These values represent the bulk ionic conductivities of the SE.[36] The low electrical conductivities of the SE led to high charge transfer resistances (R_{CT}), which explains the absence of prominent semi-circular shapes.[37] For Mg, the emergence of a semi-circle corresponding to the SEI resistance (R_{SEI}) at high frequencies after cycling indicated SEI formation as a result of side reactions between the Li deposited during charging and the SE (Fig. 3(c)).[38,39] Additionally, the pronounced semi-circle corresponding to R_{CT} reflected Li filament growth within the SE layer. By contrast, in the case of W/Mg, the semi-circle corresponding to R_{SEI} could not be retrieved and the graph was more vertical than that of Mg (Fig. 3(d)). The EIS results obtained after 25 and 50 cycles exhibited a consistent trend (Fig. S14, ESI†). This again implies that the presence of the W layer restricted SEI formation and inhibited Li dendritic growth to mitigate the accumulation of byproducts within the cell.

Inhibition of dendritic growth and effect on CCD

Following the 100-cycle half-cell evaluation, XRM with μ-CT was employed to visualize the three-dimensional (3D) anode–SE interfaces[40,41] (Fig. S15, ESI†). Voids stemming from Li dendritic growth are clearly visible in the SE layer of the Mg sample (Fig. 4(a)). This implies that, even though Mg may successfully

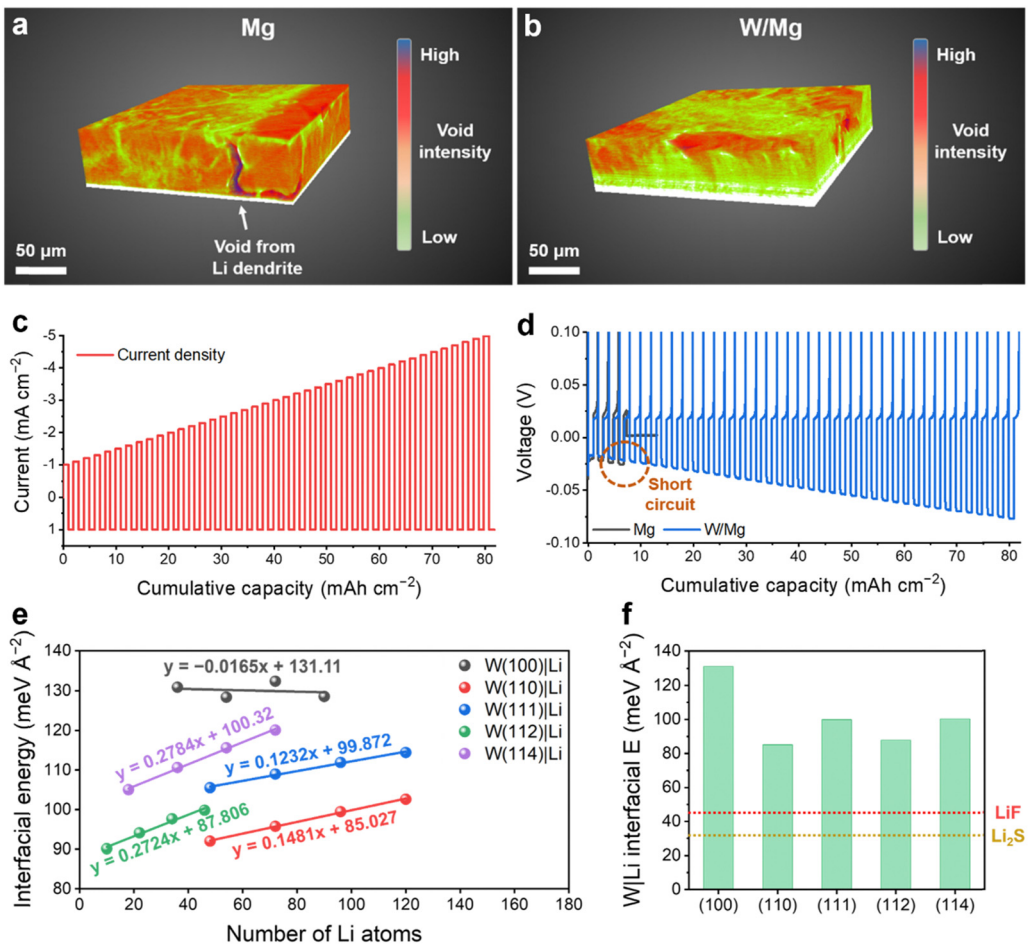

Fig. 4 Effect of W layer on the inhibition of Li dendrite penetration. (a) and (b) XRM 3D images of anode–SE interfaces using the (a) Mg and (b) W/Mg thin-films after 100 cycles in half-cells. The white areas at the bottom represent the anode current collectors and the colored regions on top correspond to the SE layers. (c) Current densities used in the Li plating CCD test with a fixed capacity of 1 mA h cm^{-2}. Negative and positive values represent Li plating and stripping processes, respectively. The plating current density was increased from 1 mA cm^{-2} in increments of 0.1 mA cm^{-2}, whereas the stripping current density was held constant at 1 mA cm^{-2}. (d) Voltage *vs.* cumulative capacity profiles of the corresponding Li plating CCD test of the thin-film electrodes. (e) and (f) DFT calculations of the interfacial energies between W and Li. (e) Interfacial energy as a function of the number of Li atoms. (f) Calculated Li interfacial energies for various crystallographic planes of W. W exhibits a significantly higher Li interfacial energy across all crystallographic orientations compared to LiF, the common SEI component in LIBs, and Li_2S, the prevalent SEI component in ASSBs.

nucleate Li, the Mg layer alone is insufficient to entirely prevent extensive Li dendritic growth. In contrast, for W/Mg, voids connected to the white anode current collector were not detected (Fig. 4(b)). The 3D XRM results were used to generate 2D representations at the anode–SE contacts for both cells (Fig. S16, ESI†). These images are clearly distinct in that the electrode with the W/Mg layers has a flat and uniform interface with hardly any voids, contrary to the electrode with Mg, of which the interface has multiple large voids. Furthermore, cross-sectional examination of the W/Mg electrode following 100 half-cell cycles, revealed the persistence of the bilayer structure with W on top of Mg (Fig. S17, ESI†). A subsequent cross-sectional analysis following Li deposition in the 101st cycle further confirmed the preservation of each layer's integrity (Fig. S18, ESI†).

The durability of the protective layer was additionally evaluated at high current densities by specifically focusing on the critical current density (CCD) for Li plating. Using the test protocol shown in Fig. 4(c), the CCD for the Mg electrode was determined as 1.3 mA cm^{-2}. In contrast, the CCD dramatically increased for the W/Mg electrode, without any short-circuiting until 5.0 mA cm^{-2} (Fig. 4(d)). The conspicuously different CCD values imply that the addition of the 30 nm-thick W layer markedly enhanced the tolerance against high current density, one of the greatest challenges presented by ALASSB operation. Given that the CCD values for sulfide SEs in typical Li symmetric

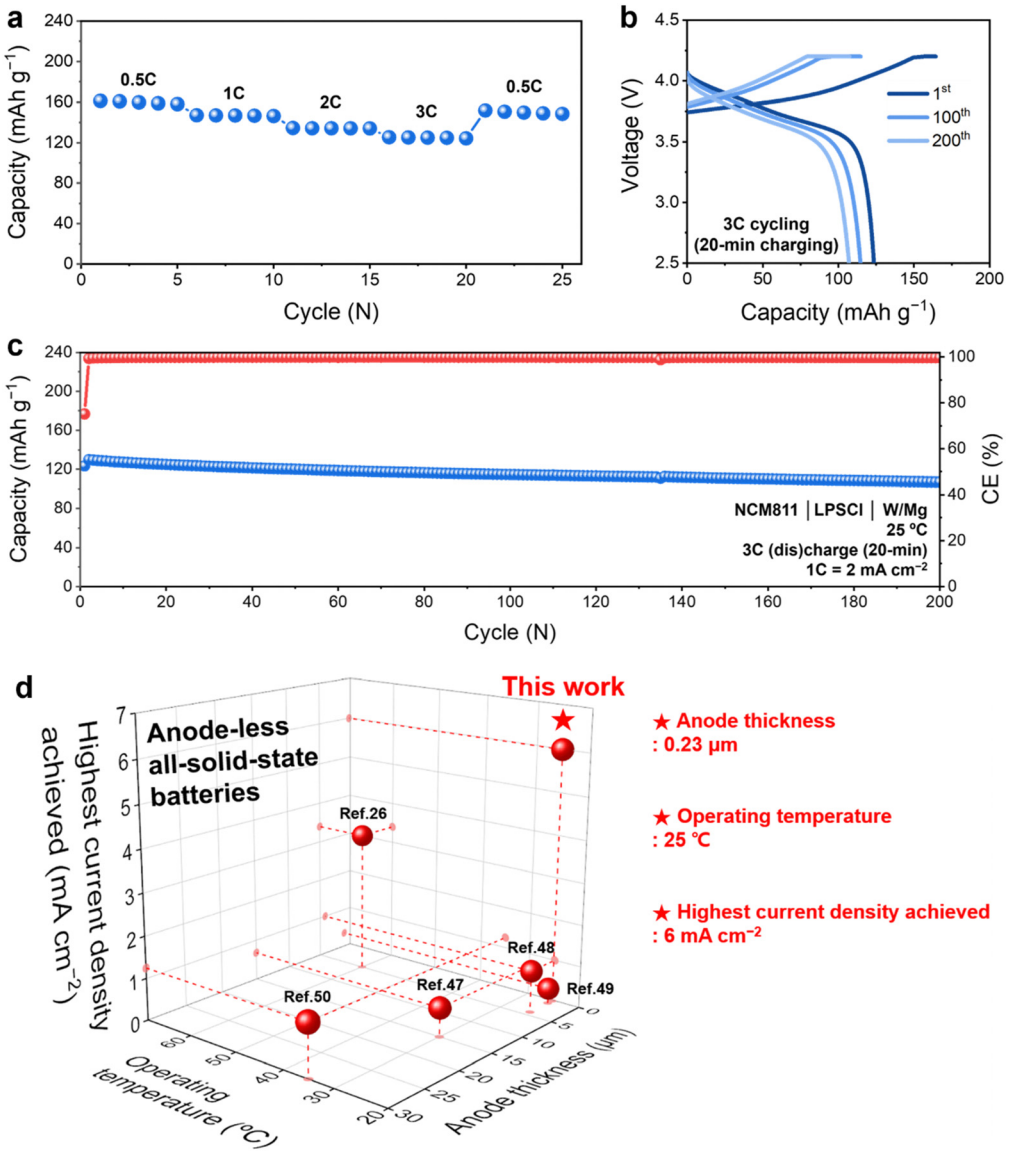

Fig. 5 Full-cell evaluations of the W/Mg thin-film anode paired with an NCM811 cathode. (a) Assessment of charging capability by varying the charge rate while fixing the discharge rate at 0.5C (1 mA cm^{-2}). Areal capacity = 2 mA h cm^{-2}. (b) and (c) Examination of charge–discharge cycling at 3C (6 mA cm^{-2}) with a 20-min time cutoff during charge and 2.5 V voltage cutoff during discharge. (b) Voltage profiles and (c) capacity retention (blue) and coulombic efficiency (red) during cycling. (d) Comparison of the anode layer thickness, operating temperature, and highest current density with those of previously reported ALASSB full-cells.

cells are usually approximately 1 mA cm^{-2}, the achieved CCD value of 5.0 mA cm^{-2} for Li plating is remarkable.[42]

Aiming to comprehensively understand the ability of W to effectively curb the growth of Li dendrites, we conducted density functional theory (DFT) calculations to assess the Li interfacial energy of W (Fig. 4(e) and (f)). These calculations spanned the intrinsic crystallographic planes of W, including those perpendicular to the predominant (110) plane. The relationship between the interfacial energy and quantity of Li atoms is plotted in Fig. 4(e), with the interfacial energy determined from the *y*-intercept of the fitted line. A negative Li interfacial energy indicates a spontaneous chemical reaction, a characteristic commonly observed for various sulfide SEs due to their narrow electrochemical stability windows.[43] Indeed, the computed Li interfacial energy of the argyrodite-type LPSCl SE employed in this work was remarkably low, measuring −33.767 meV $Å^{-2}$ for the (100) plane (Fig. S19, ESI†). This underscores the effectiveness of using a protective layer with high Li interfacial energy at the anode–SE interface and the ability of this layer to prevent the interfacial degradation of the sulfide SE by the Li metal. The Li interfacial energy of representative SEI components was also systematically calculated (Fig. S20, ESI†). Li_2S, a representative SEI component of sulfide SEs, demonstrated a Li interfacial energy of 31.678 meV $Å^{-2}$. This value is considerably higher than that of the LPSCl SE, and is indicative of the effective passivation of the SEI at the anode interface. Additionally, LiF, widely reported to be an optimal SEI component of lithium-ion batteries (LIBs), exhibited relatively high interfacial energy of 44.054 meV $Å^{-2}$. Indeed, researchers focusing on both LIBs and ASSBs are actively pursuing ways to uniformly integrate LiF components into the SEI to protect the interface.[44,45] Calculations of the Li interfacial energies of various crystallographic planes of W revealed that the interfacial energy of W is significantly higher than that of LiF across all planes (Fig. 4(f)). This substantiates the idea that the use of a 30 nm-thick W layer to increase the CCD to such a remarkable extent can be attributed to the exceptionally high Li interfacial energy of W, which induces uniform Li plating underneath.

High-energy and fast-(dis)charging ASSB

Subsequently, the W/Mg thin-film anode was evaluated in a full-cell by employing $LiNbO_3$-coated $LiNi_{0.8}Co_{0.1}Mn_{0.1}O_2$ (NCM811) as the cathode active material. Initially, the discharge capacity reached 193 mA h $g_{cathode}^{-1}$ during the first cycle at 0.1C, along with a high initial coulombic efficiency (ICE) of 92.3% (Fig. S21, ESI†). The evaluation was succeeded by a rate assessment in which the charge current density was increased sequentially from 0.5C to 1C, 2C, and 3C, while the discharge current density was kept constant at 0.5C (Fig. 5(a)). Remarkably, the charge and discharge profiles of the W/Mg-based full-cell were stable up to 3C (corresponding to 6 mA cm^{-2}) without internal short circuits. In sharp contrast, its Mg-based full-cell counterpart experienced internal short circuits even at 1C as the cell showed infinite charging behavior[46] (Fig. S22, ESI†). The high-rate charging capability resulting from implementation of the lithio-amphiphilic bilayer was preserved in the prolonged cycling tests at the high C-rate (Fig. 5(b) and (c)). When cycled at 3C for both charging and discharging, with a 20-minute cutoff time for charging, the W/Mg-based full-cell delivered stable cycling performance for 200 cycles with capacity retention of 86.7%. This retention corresponds to capacity loss of only 0.06658% per cycle. The CE exceeded 99.9% at only the 15th cycle and the average CE for 200 cycles was as high as 99.7%. In comparison with other ALASSB results[26,47–50] reported to date,

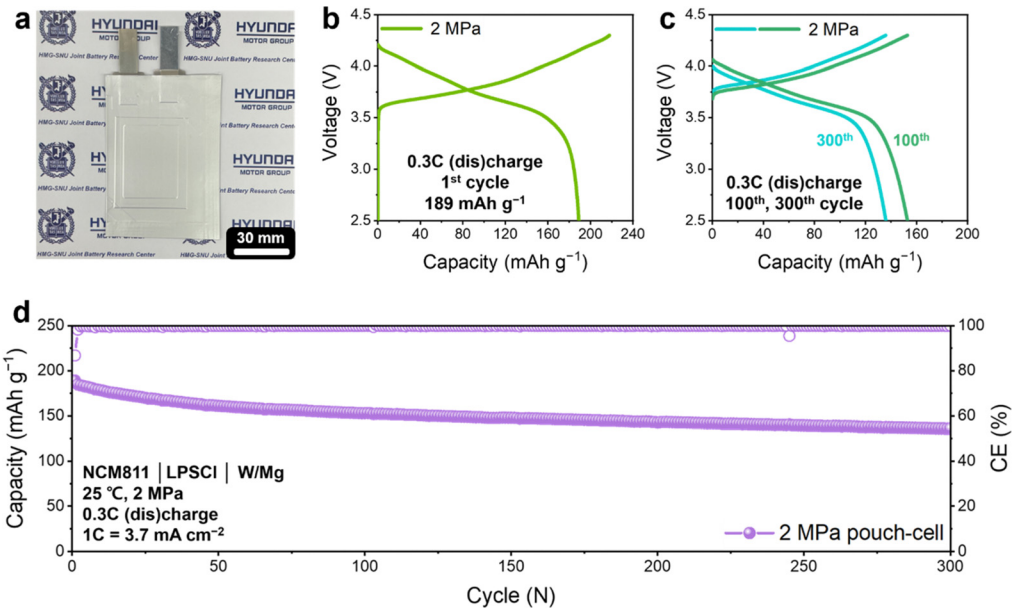

Fig. 6 High-energy density pouch-cell evaluations at room temperature (25 °C) and low pressure (2 MPa). (a) Photograph of the W/Mg-based pouch-cell. (b) and (c) Voltage profiles of the (b) 1st, (c) 100th, and 300th cycles. (d) Cycle life of the corresponding pouch-cells at a current density of 0.3C (1C = 3.7 mA cm^{-2}).

the W/Mg-based full-cell delivered highly competitive performance in terms of the anode thickness, operating temperature, and highest current density achieved without short circuiting (Fig. 5(d)). This comparison emphasizes that the lithio-amphiphilic nanobilayer concept in this study represents a useful design principle for the anode protection layer in ALASSBs without sacrificing the advantage of high energy density originating from the anode-less cell configuration.

Influence of the thickness of the W layer and presence of the Mg layer

The extent to which the thickness of the W layer influences the performance of the W/Mg electrode was investigated by depositing W and Mg layers that were both 200 nm thick (W(200 nm)/Mg(200 nm)). This electrode consistently displayed voltage dips during repeated Li depositions when tested in Li metal half-cells (Fig. S23, ESI†). Intriguingly, in this cell, the increased thickness of the W layer rendered Li ion diffusion infeasible, resulting in the predominant reduction of Li ions on the lithiophobic W layer rather than on the underlying Mg layer. Subsequent cross-sectional SEM-EDS analysis corroborated our interpretation of the observed voltage dips, namely that all the Li was exclusively deposited on top of the W layer, instead of on the Mg layer underneath (Fig. S24, ESI†). The thickness of the W layer should be appropriately controlled in nanoscale to beneficially utilize its lithiophobicity toward keeping the Li deposits highly condensed by effectively suppressing unwanted dendritic Li growth.

Additionally, an electrode with a 30 nm-thick W thin-film without a Mg layer (W(30 nm)/Mg(0 nm)) was fabricated to systematically assess the impact of the lithiophilic Mg layer. In this case, the absence of lithiophilic Li nucleation seeds resulted in recurrent nucleation overpotential, manifested as voltage dips (Fig. S25, ESI†), and provided evidence of Li nucleation on the lithiophobic substrate. Moreover, cross-sectional analysis revealed that all the Li was deposited on top of the W layer (Fig. S26, ESI†). These experiments reconfirmed the thermodynamic Li attraction of Mg based on its

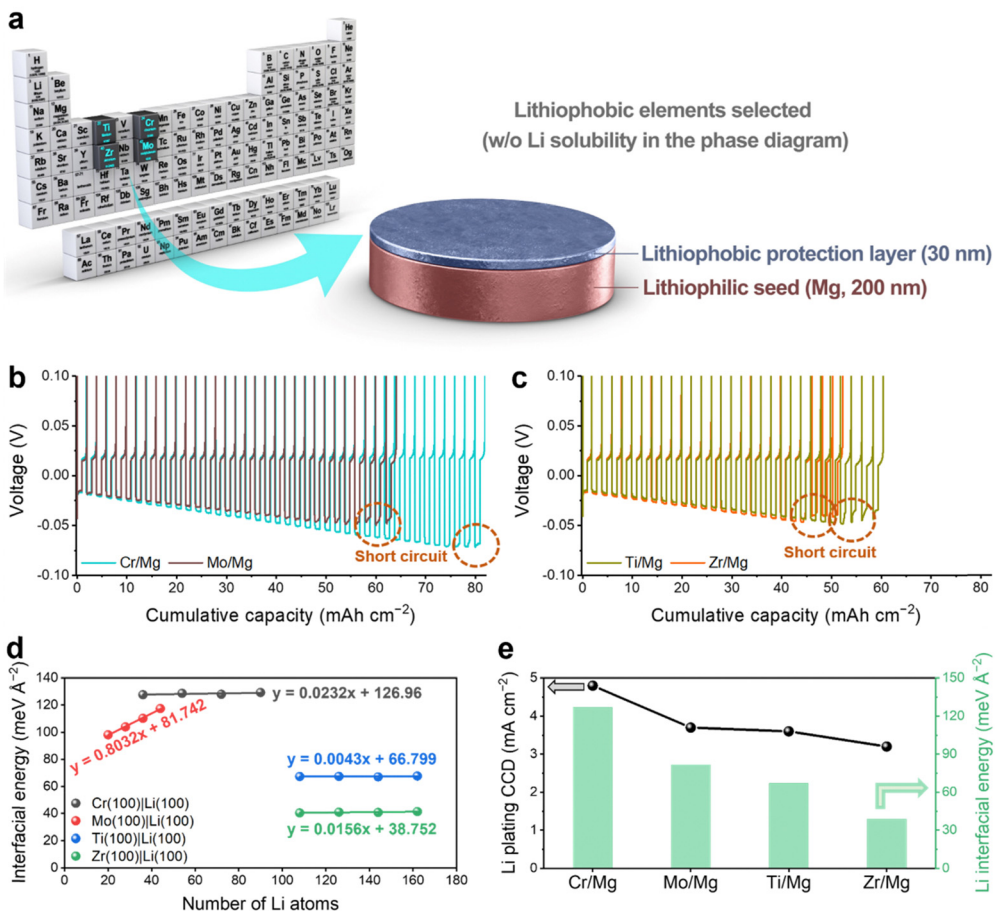

Fig. 7 Relationship between Li plating CCD and Li interfacial energy of the protective layer. (a) Schematic illustration of the selection of lithiophobic metals from among various transition metals based on their Li solubility according to their respective phase diagrams. (b) and (c) Voltage *vs.* cumulative capacity profiles of the X/Mg (X = Cr, Mo, Ti, and Zr) thin-film electrodes in Li half-cells to determine their CCD values. The plating current density starts at 1 mA cm^{-2} and increases in increments of 0.1 mA cm^{-2}, while the stripping current density remains fixed at 1 mA cm^{-2}. (d) DFT-calculated Li interfacial energies of various lithiophobic metals as a function of the number of Li atoms. (e) Correlation between Li interfacial energies of X in X/Mg and Li plating CCD values.

high lithiophilicity and that the W and Mg layers both uniquely contribute toward stabilizing Li (de)plating at practically viable temperature and pressure levels.

Low-pressure pouch-cell assessments

The feasibility of operating W/Mg in practically viable cell settings was evaluated using pouch-type full-cells (Fig. 6(a)). These tests were intended to approximate real operating conditions as closely as possible (room temperature (25 °C), low stack pressure (2 MPa), and anode-less cell configuration). Thus far, to the best of our knowledge, only a single study[29] reported meeting all of these criteria concurrently. However, the given study employed current densities as low as 0.1 C, and the capacity retention was only 57.9% after 30 cycles. In comparison, the W(30 nm)/Mg(200 nm)-based pouch cells achieved initial discharge capacities of 189 mA h $g_{cathode}^{-1}$ at 0.3C (Fig. 6(b)). With a high areal capacity of 3.7 mA h cm^{-2} and a current density of 0.3C, long-term cycle evaluations attested to decent performance. The voltage profiles remained stable without any evidence of short-circuiting (Fig. 6(c)) and the capacity retention after 300 cycles was 71.9% (Fig. 6(d)). Moreover, the CE surpassed 99.9% at the 4th cycle and exceeded 99.99% at the 9th cycle. When evaluated at a higher current density of 1C (3.7 mA h cm^{-2}), the system continued to exhibit robust performance (Fig. S27, ESI†). The calculated volumetric energy density of the W/Mg-based pouch cell (Fig. S28, ESI†) reached 1100 W h L^{-1} (Table S1, ESI†) and revalidated the impact of the extreme thinness of the anode.

Extension to various lithiophobic elements

The broad applicability of the concept of lithio-amphiphilicity was assessed by evaluating the performance of other lithiophobic metals, including chromium (Cr), molybdenum (Mo), titanium (Ti), and zirconium (Zr), based on their inability to form Li alloys according to their respective phase diagrams. Thin-films with a uniform thickness of 30 nm were deposited on Mg (Fig. 7(a)), in accordance with the above-mentioned deposition of W. Half-cell plating-stripping evaluations of these X (30 nm)/Mg (200 nm) (X = Cr, Mo, Ti, and Zr) thin-film electrodes confirmed Li nucleation on the Mg layer as indicated by the disappearance of the voltage dips from the 2nd cycle onwards, thereby mirroring the behavior of W/Mg (Fig. S29, ESI†). Accordingly, the CCD values for Li plating across these thin-films exceeded 3.2 mA cm^{-2} to affirm the universality of the X/Mg bilayer strategy (Fig. 6(b) and (c)). In particular, the CCD value of Cr/Mg was as high as 4.8 mA cm^{-2}, in comparison with the baseline CCD of 1.3 mA cm^{-2} for bare Mg. Additionally, the higher Li interfacial energies of these four lithiophobic metals (DFT results in Fig. S30, ESI†) than those of the representative SEI components (values in Fig. 4(f)) validate the effectiveness of incorporating nanoscale layers of these metals into anodes to mitigate Li dendrite formation. Notably, the highest values of the interfacial energy, those against the Li (100) plane, followed the order of Cr > Mo > Ti > Zr (Fig. 7(d)), which indeed corresponds well with the CCD value for Li plating (Fig. 7(e)). These consistent trends reconfirm the validity of using the Li interfacial energy as a metric for designing the lithio-amphiphilic nanobilayer. The comparison of the CCD values indicates that there might exist a threshold (*i.e.*, 100 meV A^{-2}) in terms of Li interfacial energy in evaluating the CCD value. As counter-examples, Mo and Ti with different Li interfacial energies (81.742 *vs.* 66.799 meV A^{-2}) showed almost identical CCD values as their Li interfacial energies are below the threshold.

Conclusions

In spite of the unprecedented theoretical energy density from the inherent cell configuration of ALASSBs, short circuit-free reliable operation at practically viable temperature and stack pressure levels remains challenging and few attempts have been reported. Our approach was to introduce a lithio-amphiphilic nanobilayer with a total thickness of only 230 nm. The key feature thereof is the thinness of the W layer, which allows facile Li ion transport through this layer. In addition, its high interfacial energy with metallic Li serves to enable Li deposits to coalesce toward a highly compact morphology, thus protecting the anode from the uncontrolled growth of Li dendrites and side reactions with the SE. Simultaneously, the lithiophilic Mg layer underneath the W promotes uniform Li (de)plating through its nucleation with Li. All of these physicochemical properties synergistically allow the ALASSB cell to achieve CCD that exceeds 5.0 mA cm^{-2} and to operate stably at room temperature and low stack pressure. In a broader context, the demonstrated strategies are universally applicable to other transition metals with negligible Li solubility as well as other high energy density anodes that are susceptible to Li dendritic growth under highly polarized operating conditions.

Author contributions

J. O. and J. W. C. conceived and planned the research. J. O., S. H. C., J. Y. K., G.-J. L., and K. Y. B. carried out the pouch-cell evaluations. H.K. performed the DFT calculations for the Li interfacial energy. J. O., T. L., N. L., Y. S., and W. J. C. conducted sample characterizations and electrochemical measurements. J. O. and J. W. C. co-wrote the manuscript. J. W. C. supervised the research. All authors participated in discussions of the results and commented on the manuscript.

Data availability

The data supporting the findings of this study are available within the article and its ESI.† Additional datasets generated and analyzed during the current study are available from the corresponding author on reasonable request. No software or code have been included as part of this study.

Conflicts of interest

The authors declare no competing interests.

Acknowledgements

J. W. C. acknowledges support from the Swiss National Science Foundation (SNF) (grant no. Sinergia CRSII5_202296), the National Research Foundation of Korea (NRF) (grant no. NRF-2022M3J1A1054151 and RS-2023-00261543), and generous support from the Institute of Engineering Research (IOER) and Research Institute of Advanced Materials (RIAM) at Seoul National University. This work was also supported by Hyundai Motor Company.

References

1 M. Armand and J. M. Tarascon, *Nature*, 2008, **451**, 652–657.
2 J. W. Choi and D. Aurbach, *Nat. Rev. Mater.*, 2016, **1**, 16013.
3 J. M. Tarascon and M. Armand, *Nature*, 2001, **414**, 359–367.
4 J. Janek and W. G. Zeier, *Nat. Energy*, 2016, **1**, 16141.
5 C. Arbizzani, G. Gabrielli and M. Mastragostino, *J. Power Sources*, 2011, **196**, 4801–4805.
6 R. Gond, W. van Ekeren, R. Mogensen, A. J. Naylor and R. Younesi, *Mater. Horiz.*, 2021, **8**, 2913–2928.
7 J. Lee, T. Lee, K. Char, K. J. Kim and J. W. Choi, *Acc. Chem. Res.*, 2021, **54**, 3390–3402.
8 H.-J. Deiseroth, S.-T. Kong, H. Eckert, J. Vannahme, C. Reiner, T. Zaiß and M. Schlosser, *Angew. Chem., Int. Ed.*, 2008, **47**, 755–758.
9 Z. Zhang, Y. Shao, B. Lotsch, Y.-S. Hu, H. Li, J. Janek, L. F. Nazar, C.-W. Nan, J. Maier, M. Armand and L. Chen, *Energy Environ. Sci.*, 2018, **11**, 1945–1976.
10 R. C. Xu, X. L. Wang, S. Z. Zhang, Y. Xia, X. H. Xia, J. B. Wu and J. P. Tu, *J. Power Sources*, 2018, **374**, 107–112.
11 F. Zheng, M. Kotobuki, S. Song, M. O. Lai and L. Lu, *J. Power Sources*, 2018, **389**, 198–213.
12 N. Kamaya, K. Homma, Y. Yamakawa, M. Hirayama, R. Kanno, M. Yonemura, T. Kamiyama, Y. Kato, S. Hama, K. Kawamoto and A. Mitsui, *Nat. Mater.*, 2011, **10**, 682–686.
13 N. Mahmood, T. Tang and Y. Hou, *Adv. Energy Mater.*, 2016, **6**, 1600374.
14 P. Oh, J. Yun, J. H. Choi, K. S. Saqib, T. J. Embleton, S. Park, C. Lee, J. Ali, K. Ko and J. Cho, *Angew. Chem., Int. Ed.*, 2022, **61**, e202201249.
15 J. A. Lewis, K. A. Cavallaro, Y. Liu and M. T. McDowell, *Joule*, 2022, **6**, 1418–1430.
16 Y. P. Wu, E. Rahm and R. Holze, *J. Power Sources*, 2003, **114**, 228–236.
17 C. Heubner, S. Maletti, H. Auer, J. Hüttl, K. Voigt, O. Lohrberg, K. Nikolowski, M. Partsch and A. Michaelis, *Adv. Funct. Mater.*, 2021, **31**, 2106608.
18 S. Chen, J. Zhang, L. Nie, X. Hu, Y. Huang, Y. Yu and W. Liu, *Adv. Mater.*, 2021, **33**, 2002325.
19 N. Lee, J. Oh and J. W. Choi, *Mater. Futures*, 2023, **2**, 013502.
20 S. Nanda, A. Gupta and A. Manthiram, *Adv. Energy Mater.*, 2021, **11**, 2000804.
21 A. J. Louli, A. Eldesoky, R. Weber, M. Genovese, M. Coon, J. deGooyer, Z. Deng, R. T. White, J. Lee, T. Rodgers, R. Petibon, S. Hy, S. J. H. Cheng and J. R. Dahn, *Nat. Energy*, 2020, **5**, 693–702.
22 O. Tamwattana, H. Park, J. Kim, I. Hwang, G. Yoon, T.-H. Hwang, Y.-S. Kang, J. Park, N. Meethong and K. Kang, *ACS Energy Lett.*, 2021, **6**, 4416–4425.
23 W. Chen, R. V. Salvatierra, M. Ren, J. Chen, M. G. Stanford and J. M. Tour, *Adv. Mater.*, 2020, **32**, 2002850.
24 S. Liu, K. Jiao and J. Yan, *Energy Storage Mater.*, 2023, **54**, 689–712.
25 Y. Tian, Y. An, C. Wei, H. Jiang, S. Xiong, J. Feng and Y. Qian, *Nano Energy*, 2020, **78**, 105344.
26 Y.-G. Lee, S. Fujiki, C. Jung, N. Suzuki, N. Yashiro, R. Omoda, D.-S. Ko, T. Shiratsuchi, T. Sugimoto, S. Ryu, J. H. Ku, T. Watanabe, Y. Park, Y. Aihara, D. Im and I. T. Han, *Nat. Energy*, 2020, **5**, 299–308.
27 J. Oh, W. J. Chung, S. H. Jung, Y. Kim, Y. Lee, Y. J. Nam, S. Lee, C. H. Kim and J. W. Choi, *Energy Storage Mater.*, 2024, **71**, 103606.
28 M. Siniscalchi, J. Liu, J. S. Gibson, S. J. Turrell, J. Aspinall, R. S. Weatherup, M. Pasta, S. C. Speller and C. R. M. Grovenor, *ACS Energy Lett.*, 2022, **7**, 3593–3599.
29 J. Oh, S. H. Choi, J. Y. Kim, J. Lee, T. Lee, N. Lee, T. Lee, Y. Sohn, W. J. Chung, K. Y. Bae, S. Son and J. W. Choi, *Adv. Energy Mater.*, 2023, **13**, 2301508.
30 J. Sangster and A. D. Pelton, *J. Phase Equilib.*, 1991, **12**, 203.
31 P. Verma, P. Maire and P. Novák, *Electrochim. Acta*, 2010, **55**, 6332–6341.
32 V. Raj, V. Venturi, V. R. Kankanallu, B. Kuiri, V. Viswanathan and N. P. B. Aetukuri, *Nat. Mater.*, 2022, **21**, 1050–1056.
33 N. Lee, J. Lee, T. Lee, J. Oh, I. Hwang, G. Seo, H. Kim and J. W. Choi, *ACS Appl. Mater. Interfaces*, 2023, **15**, 34931–34940.
34 F. Strauss, D. Stepien, J. Maibach, L. Pfaffmann, S. Indris, P. Hartmann and T. Brezesinski, *RSC Adv.*, 2020, **10**, 1114–1119.
35 X. Ji, S. Hou, P. Wang, X. He, N. Piao, J. Chen, X. Fan and C. Wang, *Adv. Mater.*, 2020, **32**, 2002741.
36 P. Vadhva, J. Hu, M. J. Johnson, R. Stocker, M. Braglia, D. J. L. Brett and A. J. E. Rettie, *ChemElectroChem*, 2021, **8**, 1930–1947.
37 H.-K. Tian and Y. Qi, *J. Electrochem. Soc.*, 2017, **164**, E3512.
38 L. Wang, J. Zhao, X. He, J. Gao, J. Li, C. Wan and C. Jiang, *Int. J. Electrochem. Sci.*, 2012, **7**, 345–353.
39 L. Braks, J. Zhang, A. Forster, P. W. Fritz, J. Oh, M. El-Kazzi, J. W. Choi and A. Coskun, *Angew. Chem., Int. Ed.*, 2024, e202408238.
40 J. Oh, S. H. Choi, B. Chang, J. Lee, T. Lee, N. Lee, H. Kim, Y. Kim, G. Im, S. Lee and J. W. Choi, *ACS Energy Lett.*, 2022, **7**, 1374–1382.
41 P. R. Shearing, N. P. Brandon, J. Gelb, R. Bradley, P. J. Withers, A. J. Marquis, S. Cooper and S. J. Harris, *J. Electrochem. Soc.*, 2012, **159**, A1023.
42 F. Han, J. Yue, X. Zhu and C. Wang, *Adv. Energy Mater.*, 2018, **8**, 1703644.
43 K. J. Kim, M. Balaish, M. Wadaguchi, L. Kong and J. L. M. Rupp, *Adv. Energy Mater.*, 2021, **11**, 2002689.

44 T. Li, X.-Q. Zhang, P. Shi and Q. Zhang, *Joule*, 2019, **3**, 2647–2661.
45 Y. Liu, X. Tao, Y. Wang, C. Jiang, C. Ma, O. Sheng, G. Lu and X. W. Lou, *Science*, 2022, **375**, 739–745.
46 J. A. Lewis, C. Lee, Y. Liu, S. Y. Han, D. Prakash, E. J. Klein, H.-W. Lee and M. T. McDowell, *ACS Appl. Mater. Interfaces*, 2022, **14**, 4051–4060.
47 S. H. Park, D. Jun, G. H. Lee, S. G. Lee, J. E. Jung, K. Y. Bae, S. Son and Y. J. Lee, *Adv. Sci.*, 2022, **9**, 2203130.
48 J. Lee, S. H. Choi, G. Im, K.-J. Lee, T. Lee, J. Oh, N. Lee, H. Kim, Y. Kim, S. Lee and J. W. Choi, *Adv. Mater.*, 2022, **34**, 2203580.
49 Y. Wang, Y. Liu, M. Nguyen, J. Cho, N. Katyal, B. S. Vishnugopi, H. Hao, R. Fang, N. Wu, P. Liu, P. P. Mukherjee, J. Nanda, G. Henkelman, J. Watt and D. Mitlin, *Adv. Mater.*, 2023, **35**, 2206762.
50 X. Xing, Y. Li, S. Wang, H. Liu, Z. Wu, S. Yu, J. Holoubek, H. Zhou and P. Liu, *ACS Energy Lett.*, 2021, **6**, 1831–1838.